

# Resolving electron scale turbulence in spherical tokamaks with flow shear

W. Guttenfelder<sup>1,a)</sup> and J. Candy<sup>2</sup>

<sup>1</sup>Centre for Fusion, Space, and Astrophysics, Department of Physics, University of Warwick, Coventry CV4 7AL, United Kingdom

<sup>2</sup>General Atomics, P.O. Box 85608, San Diego, CA 92186-5608, USA

(Received 22 September 2010; accepted 6 January 2011; published online 16 February 2011)

This paper presents nonlinear gyrokinetic simulations of electron temperature gradient (ETG) turbulence based on spherical tokamak (ST) parameters. Most significantly the simulations include the strong toroidal flow and flow shear present in STs that suppress ion-scale turbulence while using kinetic ions at full mass ratio ( $m_i/m_e=3600$ ). The flow shear provides a physical long-wavelength cutoff mechanism that aids saturation of the simulations, which has previously been demonstrated to be problematic depending on magnetic shear. As magnetic shear varies widely in STs we systematically demonstrate saturation and convergence of the ETG simulations with respect to grid resolution, physical domain size, and boundary conditions. While using reduced ion mass or adiabatic ions can lessen computational expense they do not always provide reliable results. The resulting spectra from converged simulations are anisotropic everywhere in contrast to previous ETG simulations without flow shear. These results have implications for interpreting turbulence measurements, and represent an important step in determining when and where ETG turbulence is expected to be relevant in ST plasmas. They are also important in the context of validating simulations with both experimental transport analysis and turbulence measurements.

© 2011 American Institute of Physics. [doi:10.1063/1.3551701]

## I. INTRODUCTION

While ion thermal transport in spherical tokamaks (STs) can approach the level of neoclassical theory, electron thermal transport is almost always anomalous.<sup>1–3</sup> As a consequence of NBI heating, driven toroidal flows generate significant  $E \times B$  shear which can largely suppress low-frequency ion-scale turbulence driven by ion temperature gradient (ITG) or trapped electron mode (TEM) instabilities.<sup>4,5</sup> In regions of the plasma where sufficient gradients exist, electron temperature gradient (ETG) driven turbulence is a candidate for anomalous transport, although ETG cannot explain the large transport observed in discharges with flat central  $T_e$  profiles at higher NBI power.<sup>6</sup> Even though the transport spectrum in multiscale turbulence simulations<sup>7,8</sup> is continuous from ion to electron scales, it is useful to think of ITG/TEM turbulence as that which inhabits the range  $k_\theta \rho_i \lesssim 1$ , and ETG turbulence as dominant for  $k_\theta \rho_i \gtrsim 1$ , where  $k_\theta \doteq nq/r$ . But strictly speaking, ETG turbulence only becomes fully decoupled from the ion dynamics for much higher wavenumbers, in the range  $k_\theta \rho_e \gtrsim 0.1$ .<sup>8</sup> Note that  $\rho_i \approx 60\rho_e$  for a deuterium plasma. Here,  $\rho_a = v_{ta}/\Omega_a$  is the gyroradius,  $v_{ta} = \sqrt{T_a/m_a}$  is the thermal velocity,  $\Omega_a = e_a B_{\text{unit}}/(m_a c)$  is the effective cyclotron frequency (the cyclotron frequency evaluated at the effective field,  $B_{\text{unit}}$ , defined in Ref. 9), and the subscript  $a$  is the species index. To make connection with previous work, we also define the ion-sound gyroradius,  $\rho_s = c_s/\Omega_a$ , where  $c_s = \sqrt{T_e/m_i}$ , although in the present work  $c_s = v_{ti}$ . High- $k$  scattering measurements in NSTX<sup>10,11</sup> sometimes exhibit characteristics consistent with

ETG turbulence, often being correlated with the local  $T_e$  gradient. Because they are driven at high frequencies in the range  $v_{te}/a$ , where  $a$  is the plasma minor radius, ETG modes are not expected to be completely suppressed by  $E \times B$  shear, although recent experimental evidence suggests that this is possible.<sup>12</sup> In addition to turbulence measurements, there has been some limited success in predicting electron temperature profiles using theory-based transport models<sup>13–15</sup> illustrating that ETG is likely a relevant transport mechanism, at least in some ST regimes. These two observations lead us to further pursue physically comprehensive ETG simulations for STs.

Previously, computationally expensive multiscale simulations, using kinetic ions and electrons at reduced mass ratio,  $20 \leq \mu \leq 30$ , where  $\mu \doteq \sqrt{m_i/m_e}$ , have considered cases for which transport is dominant at ion scales, with contributions in the range  $k_\theta \rho_i > 1$  no more than 7%–15% of the total. However, this observation is predicated on the existence of some long-wavelength turbulence, and when the ion scales are weakly driven,<sup>8,16,17</sup> the electron scale contribution can be significantly larger. Alternatively, strong  $E \times B$  shear can reduce the total transport substantially leaving only that from electron scales.<sup>8,16</sup> In the absence of these two effects, it is not clear that ETG simulations focusing only on electron scale dynamics are physically relevant. Many reported ETG simulations utilize perpendicular box sizes large enough to capture only electron scale dynamics ( $L \sim 200\text{--}800\rho_e$ , or equivalently,  $3\text{--}13\rho_i$ ). These domain sizes exclude ion-scale dynamics which require  $L \gtrsim 48\rho_i$  for convergence. These small domain sizes may be reasonable in situations where strong  $E \times B$  shear is expected to completely suppress ion-scale turbulence (e.g., STs or transport barriers), but it is not known *a priori* how the  $E \times B$  shear influences the electron

<sup>a)</sup>Present address: Princeton Plasma Physics Laboratory, Princeton, New Jersey 08543, USA.

scale dynamics. It was also shown<sup>16</sup> that while the small-box ETG simulations could recover approximately the same level of transport at electron scales as multiscale simulations, the resulting fluctuation and transport spectra differed substantially. Therefore the similarity in transport to the more physically relevant multiscale simulations *cannot* be assumed to be a robust result. Even if the transport were reliably predicted, physically accurate spectra are desirable for validation with turbulence diagnostics.<sup>11</sup>

The adiabatic ion (ETG-ai) approximation is often made to reduce computational expense (or simply due to the lack of multiscale simulation capability) when studying ETG transport. Unfortunately this model can lead to poorly behaved results that do not saturate, exhibiting fluctuation spectra that are nearly monochromatic (i.e., not indicative of a turbulent state). This model failure has been well documented<sup>8,18–20</sup> for the cyclone base case parameters with nominal magnetic shear  $s=(r/q)dq/dr=0.8$ , with saturation occurring only for  $s<0.4$ . Additional simulations for the cyclone base case demonstrated that saturation could be obtained at  $s=0.8$  by using kinetic ions (ETG-ki) or sufficiently strong  $E \times B$  shear (ETG-ai-exb).<sup>8</sup> In conjunction with the ETG-ai saturation problem, it was demonstrated that simulations could falsely asymptote toward saturation when under-resolved in  $(k_{\theta}\rho_e)_{\max}$ ,<sup>8</sup> whereas increasing the binormal resolution recovered the unsaturated state. Similar behavior was observed in ETG-ai simulations reported for MAST,<sup>21</sup> which appeared to saturate with  $(k_{\theta}\rho_e)_{\max}<0.4$  at  $s=0.29$ . Longer runs of these simulations<sup>22</sup> found runaway growth in the transport, developing into a monochromatic spectrum. However, for these parameters it was found that including  $E \times B$  shear or electron pitch angle scattering recovered saturation at the lower binormal resolution. Even in the limit of well-behaved ETG-ai simulations,<sup>18</sup> a binormal resolution of  $(k_{\theta}\rho_e)_{\max} \geq 1.5$  may be required to reach convergence. This is in contrast to multiscale simulations which converge using  $(k_{\theta}\rho_e)_{\max} \leq 0.5$ . We are not aware of convergence in  $k_{\theta}\rho_e$  being demonstrated for physically realistic ETG dominant simulations (with strong  $E \times B$  shear).

It remains critical to demonstrate saturation *and* convergence with respect to grid resolution for ST-relevant ETG simulations, specifically in the presence of the experimentally observed strong  $E \times B$  shear. This is an important step in determining when and where ETG turbulence is expected to be relevant in present-day ST plasmas, as well as next-generation devices. It is also important in the context of quantitatively validating simulations with both experimental transport analysis and turbulence measurements. To address these issues we employ the Eulerian gyrokinetic code GYRO,<sup>23,24</sup> capable of including electromagnetic perturbations, collisions, toroidal flow and flow shear, and profile variations in equilibrium quantities. Ref. 24 gives in detail the gyrokinetic equation (Eq. 2.37), Maxwell equations (Eqs. 2.69–2.71) and the transport coefficients (Eqs. 2.71–2.75) being solved.

The remainder of this paper is structured as follows. In Sec. II we discuss the reference parameters chosen to investigate saturation and convergence in the presence of  $E \times B$  shear. As a consequence of the numerical implementation of

$E \times B$  shear in GYRO, we spend significant time verifying that the chosen BCs do not influence the results. With this established we demonstrate convergence with grid resolution through additional simulations. The viability of using adiabatic ions or reduced ion mass is investigated in Sec. III, where the influence of  $E \times B$  shear is also discussed. Some of the turbulence characteristics of the saturated and converged simulations are shown in Sec. IV in relation to recently reported high- $k$  turbulence measurements. Conclusions are presented in Sec. V.

## II. SATURATION AND CONVERGENCE

To address the issue of saturation and convergence we perform a number of simulations using kinetic electrons and ions at full mass ratio ( $\mu=60$ ). While the MHD equilibrium in GYRO can generally be specified from a numerically calculated equilibrium,<sup>9</sup> the Miller local equilibrium model<sup>25</sup> has been utilized for the following simulations. Parameters are chosen to be representative of the midradius in MAST discharges with  $<2$  MW of NBI heating (e.g., Ref. 2):  $R/a=1.6$ ,  $r/a=0.5$ ,  $\kappa=1.5$ ,  $\delta=0.2$ ,  $q=1.4$ ,  $s=0.8$ ,  $a/L_{Te}=a/L_{Ti}=3.0$ ,  $a/L_n=1.0$ , and  $T_e=T_i$ . Unless otherwise specified, both electrons and ions are gyrokinetic. Initial simulations are run in the electrostatic, collisionless limit for computational efficiency as these effects are not expected to significantly complicate convergence criteria at ETG scales. While  $\beta_e=8\pi n_e T_e/B^2$  can be relatively large near the magnetic axis in MAST ( $\beta_e \sim 0.1$ ) previous ETG simulations for midradius parameters<sup>21,22</sup> indicate the resulting nonlinear transport is rather insensitive to the inclusion of EM perturbations, although we have not verified this. Perhaps one of the biggest assumptions of unknown consequence is the neglect of the nonthermal NBI ions in the gyrokinetic model, which can account for up to 50% of the total equilibrium pressure in experiments. Investigating the influence of an energetic ion species on the ETG turbulence in STs is left for future work.

We begin using a computational domain square in the perpendicular dimensions ( $L_x=L_y=260\rho_e=4.4\rho_i$ ), with 32 toroidal modes and 128 radial grid points, giving  $(k_{\theta}\rho_e)_{\max} \approx (k_r\rho_e)_{\max} \approx 0.75$ . The resolution in parallel orbit (10 point per passing orbit) and velocity space (128 points) was previously shown to be sufficient for convergence of the transport fluxes to within about 5%–10%.<sup>26</sup> The  $E \times B$  shearing rate,

$$\gamma_E \doteq -\frac{r}{q} \frac{\partial \omega_0}{\partial r}, \quad (1)$$

was chosen to be  $\gamma_E=0.9(c_s/a)=0.015(v_{te}/a)$ , where  $\omega_0=-c \partial \Phi / \partial \psi$  is the toroidal rotation frequency, and  $\Phi$  is the (measured) equilibrium radial electric field potential. The chosen value was found to bring ETG-ai simulations in agreement with ETG-ki simulations,<sup>8</sup> but is larger than values typically found in  $<2$  MW NBI MAST discharges. The simulations here are *local* in that equilibrium density and temperature profiles, and their corresponding gradients, are held constant across the radial domain in the same way as they are in flux-tube simulations. However, due to the linear radial variation in  $E \times B$  Doppler frequency, nonperiodic

boundary conditions (BCs) on fluctuating quantities are required. Further, to minimize artificial profile relaxation in nonperiodic simulations, *buffer zones* of finite width,  $\Delta^b$ , are implemented<sup>23,24</sup> that damp the axisymmetric components of the distribution function via an effective sink rate of  $(a/c_s)v^b$ . An “adaptive source”<sup>24,27</sup> is not used here as there is no variation in the equilibrium profiles, similar to the ITG/TEM simulations in Refs. 4 and 5. For typical ion-scale simulations,  $(\Delta^b/\rho_s, av^b/c_s)=(8, 1)$  is a good choice to minimize relaxation. However it is unknown *a priori* what  $(\Delta^b, v^b)$  combination is required for these electron scale simulations.

In Fig. 1 we examine the effect of different choices of buffer parameters. The red curves use  $(\Delta^b/\rho_e, av^b/c_s)=(16, 1)$  and the black curves use  $(\Delta^b/\rho_e, av^b/c_s)=(64, 12)$ . Figure 1(a) shows radial profiles of the electron thermal diffusivity time-averaged over the last half of the simulation,  $1500 \leq (v_{te}/a)t \leq 3000$ , Fig. 1(b) shows the time-average of the flux-surface averaged perturbed temperature moment  $\langle \delta T_e \rangle_t$ , and Fig. 1(c) shows the total normalized temperature gradient

$$\left( \frac{a}{L_{Te}} \right)_{\text{total}} = \left( \frac{a}{L_{Te}} \right)_{\text{eq}} + \frac{a}{T_{e,\text{eq}}} \left( - \frac{\Delta \langle \delta T_e \rangle_t}{\Delta r} \right). \quad (2)$$

The effect of the BCs is clearly seen in all cases, such that the transport is finite and flat in the interior but approaches zero at either radial boundary. The red curve in Fig. 1(b) shows a clear trend of positive (negative) offset on the right (left) side boundary, and while the average perturbation,  $\langle \delta T_e \rangle_t / T_{e,\text{eq}} \leq 0.4\%$ , is relatively small, Fig. 1(c) shows a significant reduction (10%) in the temperature gradient in the interior of the domain. Thus, the minimal values implemented in the solid curves are clearly insufficient. For the black curves, the averaged  $\langle \delta T_e \rangle_t$  profile variation is reduced considerably in the domain interior and  $(a/L_{Te})_{\text{total}}$  is within about 0.3% of the equilibrium value. As a result, the transport has increased [Fig. 1(a)].

Figure 2 shows the time-averaged value of  $\chi_e$  versus  $(a/L_{Te})_{\text{total}}$  (averaged over the interior of the domain) for a number of simulations that independently vary buffer width  $(\Delta^b/\rho_e=16, 32, 48, 64, 80; av^b/c_s=1)$  and damping strength  $(av^b/c_s=1, 2, 4, 6, 12, 30; \Delta^b/\rho_e=64)$ . When increasing the buffer width the interior width was fixed at  $L_x^{\text{interior}}=230\rho_e$ , such that the total domain size is increased to keep resolution fixed at  $\Delta x=2\rho_e$ . For the chosen input parameters the transport is insensitive to further increases in  $(\Delta^b/\rho_e, av^b/c_s)=(64, 6)$ . The vertical lines represent the standard deviation of  $\chi_e$  during the averaging time. As a consequence of the inherent stiffness, the transport increased almost threefold for a net increase in total effective driving gradient of roughly 10%. This exercise reiterates how sensitive the resulting transport can be to perturbations that modify the effective equilibrium gradients,<sup>27</sup> an effect that must be monitored in all global codes, especially if quantitative comparisons are required.

While profile relaxation impacts the magnitude of transport, the previous simulations all saturate as expected with the use of kinetic ions and strong  $E \times B$  shear with qualita-

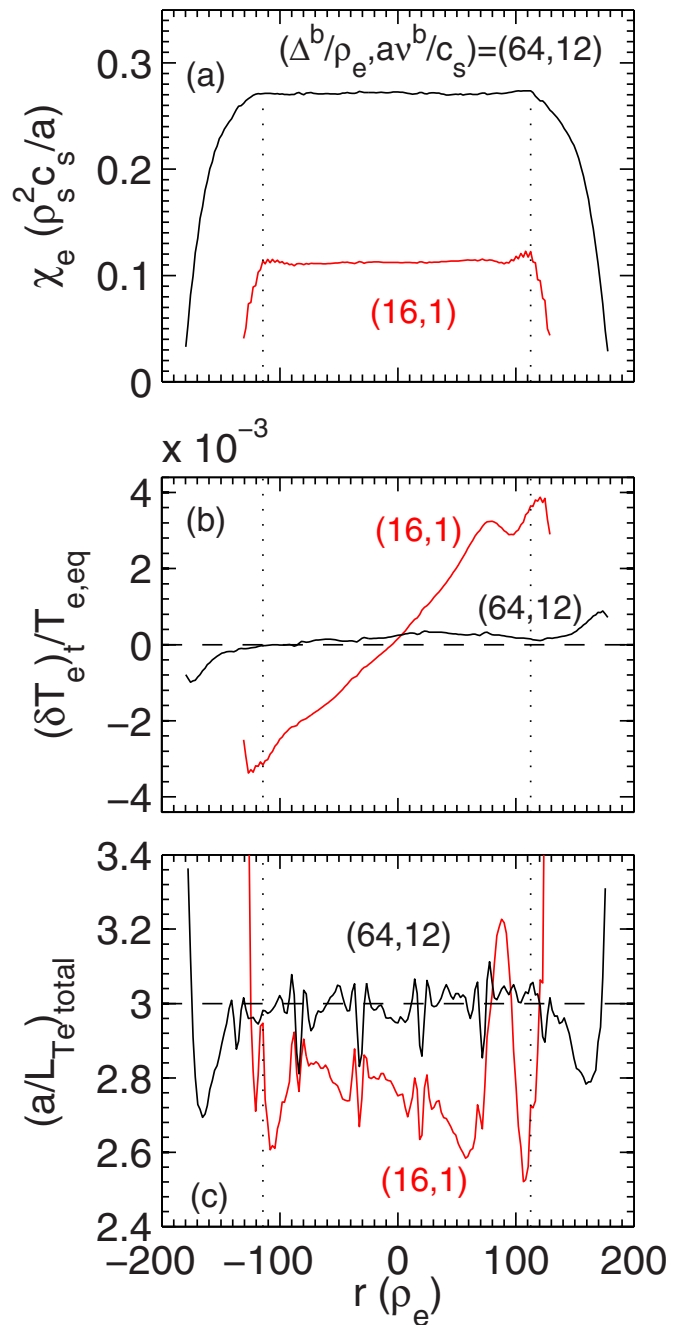


FIG. 1. (Color online) (a) Profiles of  $\chi_e$  from local GYRO simulations with  $E \times B$  shear (nonperiodic BCs) using different boundary width and damping strength. (b) Perturbed electron temperature profile (time and flux-surface averaged). (c) Total ETG profiles (including perturbations).

tively similar spectral quantities. The transport spectrum in Fig. 3 (solid black line) exhibits a clear peak at  $k_\theta \rho_e \approx 0.15$  ( $k_\theta \rho_s \approx 10$ ) with a corresponding roll-off at high  $k_\theta$  anticipated in turbulent systems. The influence of the  $E \times B$  shear is evident in the suppression of low- $k_\theta$  contributions. This low- $k_\theta$  roll-off is in contrast to most ETG simulations that exhibit a pile-up at larger scales when not simultaneously including ion scales or additional damping mechanisms. A comparable ETG simulation with  $E \times B$  shear has recently been reported using the spectral flux-tube code GS2.<sup>22</sup>

As a result of the low- $k_\theta$  cut-off provided by  $E \times B$  shear, the simulations are converged with respect to box size

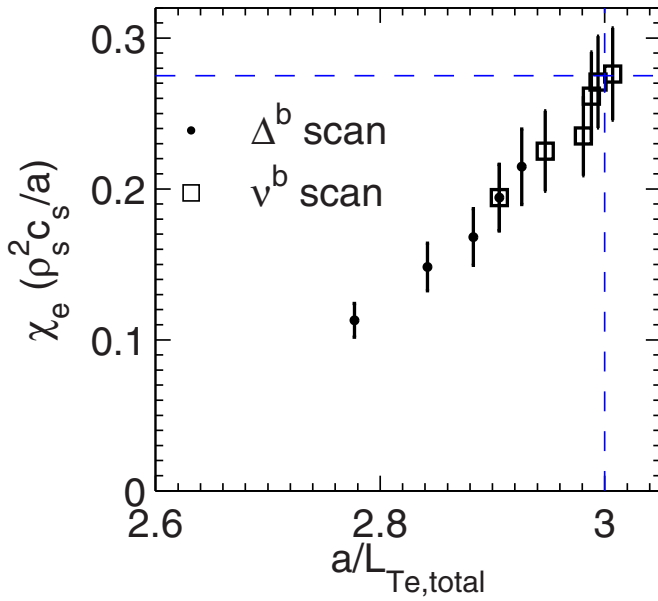


FIG. 2. (Color online)  $\chi_e$  vs.  $(a/L_{Te})_{\text{total}}$  for different boundary buffer widths ( $\Delta^b$ ) and damping rates ( $v^b$ ). Points for which  $(a/L_{Te})_{\text{total}} < 3$  indicate insufficient buffer parameters.

in both radial and binormal directions. Figure 4 shows that increasing the interior box size to  $(L_x, L_y) = (490, 400)\rho_e$  and  $(620, 530)\rho_e$  yields little change in transport (an 8% reduction). The resulting transport spectra exhibits the same low- $k_\theta$  roll-off and the radial correlation length remains unchanged ( $L_x^{\text{corr}} = 16\rho_e$  for  $C(\Delta r = L_x) = 1/e$ , as discussed below), much smaller than the radial domain width  $360 \leq L_x/\rho_e \leq 620$ . It is expected that the required binormal box size will necessarily increase as the relative strength of the  $E \times B$  shear rate decreases and ion-scale turbulence becomes more significant, as discussed in detail later. At some intermediate values of  $\gamma_E$ , it is unfortunately likely that mul-

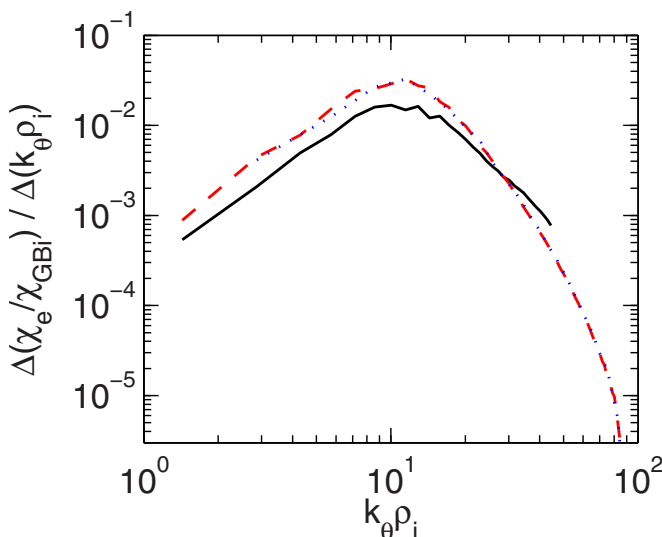


FIG. 3. (Color online) Fractional transport spectra with different binormal resolution and box size:  $L_y = 260\rho_e$ ,  $k_\theta \rho_{e,\text{max}} = 0.74$  (solid black),  $L_y = 260\rho_e$ ,  $k_\theta \rho_{e,\text{max}} = 1.5$  (dashed red),  $L_y = 130\rho_e$ ,  $k_\theta \rho_{e,\text{max}} = 1.5$  (dotted blue).

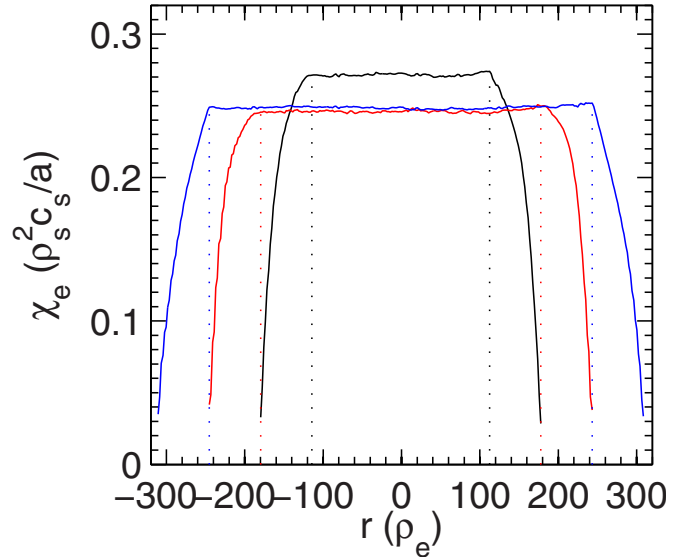


FIG. 4. (Color online) Profiles of  $\chi_e$  for different box widths.

tiscale simulations will be required to properly predict the transport and spectral properties.

Further simulations demonstrate that radial resolution,  $(k_r \rho_e)_{\text{max}} = 0.74$  is sufficient for convergence, but transport increases with binormal resolution up to  $(k_\theta \rho_e)_{\text{max}} = 1.5$ , which is equivalent to  $(k_\theta \rho_s)_{\text{max}} = 88$ . This is similar to the ETG-ai benchmark case reported in Ref. 18 although here we have included both kinetic ions and finite  $E \times B$  shear which provides a physical low- $k_\theta$  cut-off mechanism. Figure 3 shows the fractional transport spectra for the reference case  $(k_\theta \rho_e)_{\text{max}} = 0.74$  (solid black line) and a case with double the binormal resolution  $(k_\theta \rho_e)_{\text{max}} = 1.5$  (dashed red line), where the transport has increased by about 60%, from  $\chi_e = 0.26$  to  $0.42\rho_s^2 c_s / a$ . Increasing resolution another 25% to  $(k_\theta \rho_e)_{\text{max}} = 1.9$  does not change the transport. The increase occurs around the peak in the fractional transport spectra and below,  $k_\theta \rho_e < 0.3$ , while a stronger roll-off occurs in the spectra above the peak. This is in contrast to previous multiscale simulations,<sup>8,16</sup> driven strongly at ion scales in the absence of  $E \times B$  shear, that reach convergence for  $(k_\theta \rho_e)_{\text{max}} = 0.5$ .

With the low- $k_\theta$  cutoff provided by strong  $E \times B$  shear, the binormal box size can actually be reduced by a factor of 2 to  $L_y = 130\rho_e$ ,  $(k_\theta \rho_e)_{\text{max}} = 1.5$  with no effect on saturation, also illustrated in Fig. 3 (dashed blue line). The resulting quantitatively converged transport for the parameters chosen here is  $\chi_e \approx 0.4\rho_s^2 c_s / a = 8\rho_e^2 v_{Te} / L_{Te}$  which is in the range of experimental observations in both MAST and NSTX.<sup>1-3</sup> For example, at the midradius of MAST H-mode discharge 8500,<sup>2</sup>  $T_e \approx 500$  eV,  $B \approx 0.5$  T, and  $\rho_s^2 c_s / a \approx 7.6$  m<sup>2</sup>/s so that  $\chi_{e,\text{sim}} \approx 3$  m<sup>2</sup>/s compared to  $\chi_{e,\text{exp}} \approx 2$  m<sup>2</sup>/s.

We consider one final effect in this section. The above simulations were performed including only perpendicular  $E \times B$  shear. But in neutral-beam-heated MAST and NSTX discharges, the strong toroidal rotation,  $\text{Ma} \equiv v_{\text{tor}}/c_s \leq 1.0$ , gives rise to both perpendicular  $E \times B$  shear,  $\gamma_E$ , and parallel flow shear,  $\gamma_p = (qR/r)\gamma_E$ . Including the parallel shear provides an additional linear instability drive (Kelvin-Helmholtz) evident in the  $k_\theta \rho_s \leq 1$  growth rates shown in

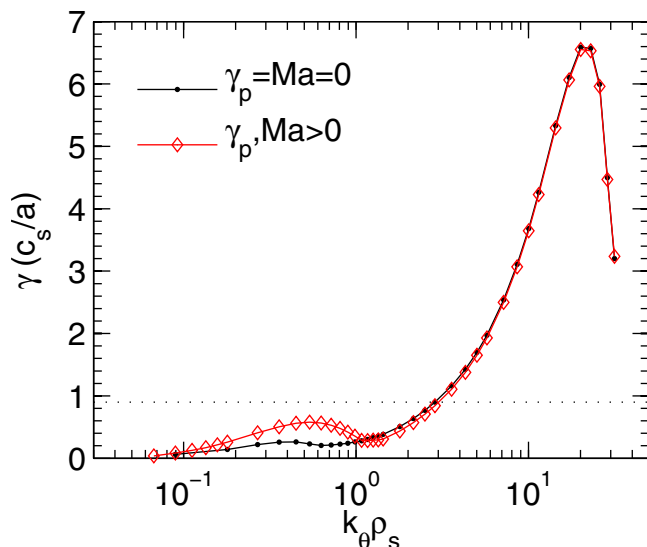


FIG. 5. (Color online) Linear growth rate spectra without (dots) and with (diamonds) toroidal flow and parallel flow shear ( $Ma$ ,  $\gamma_p$ ).

Fig. 5 ( $Ma=0.6$ ,  $\gamma_p=4.0(c_s/a)$ ,  $\gamma_E=0$ ). This increase is insufficient to overcome the  $E \times B$  shear rate (dashed line) responsible for suppression of ion-scale turbulence. Therefore it is not surprising that the resulting nonlinear ETG simulation (not shown) is unaffected by the inclusion of finite  $Ma$  and  $\gamma_p$ . This may change at different radii as the strength of the parallel flow shear is proportional to  $qR/r$ .

### III. ADIABATIC IONS, REDUCED ION MASS, AND REDUCED $E \times B$ SHEAR

#### A. Adiabatic ions

As discussed in the introduction, ETG simulations utilizing the adiabatic ion model with sufficient  $E \times B$  shear (ETG-ai-exb) were capable of reproducing the more realistic kinetic ion simulations (ETG-ki-exb), using parameters that otherwise result in nonphysical transport and spectra.<sup>8</sup> These cheaper simulations motivated the mapping of parametric dependencies ( $q$ ,  $s$ , etc.) of ETG transport in STs with strong  $E \times B$  shear.<sup>14</sup> Having now systematically demonstrated convergence for the physically relevant ETG-ki-exb simulations, we revisit adiabatic ion simulations.

Figure 6(a) shows the time trace of electron thermal diffusivity for both ETG-ki-exb and ETG-ai-exb cases using identical numerical grid and boundary parameters. In the first half of the simulation, the transport with the adiabatic ion model is identical to the kinetic ion case, within the standard deviation of the fluctuations of the time series. Near a time of  $30a/c_s$  ( $1800a/v_{Te}$ ) the transport transitions to smaller values. Before this transition occurs, the  $n=0$  zonal potential shows a gradual increase in amplitude [Fig. 6(b)] and continuously grows through the end of the simulation. The increased zonal potential intensity stems from a dominant large-wavelength ( $\lambda \sim 150\rho_e$ ) radial mode, leading to an  $E \times B$  shear rate  $v'_{E(n=0)} \approx 12v_{te}/a$  localized in the middle of the simulation domain.

As the potential and  $\delta f$  perturbations are explicitly coupled via the adiabatic ion response

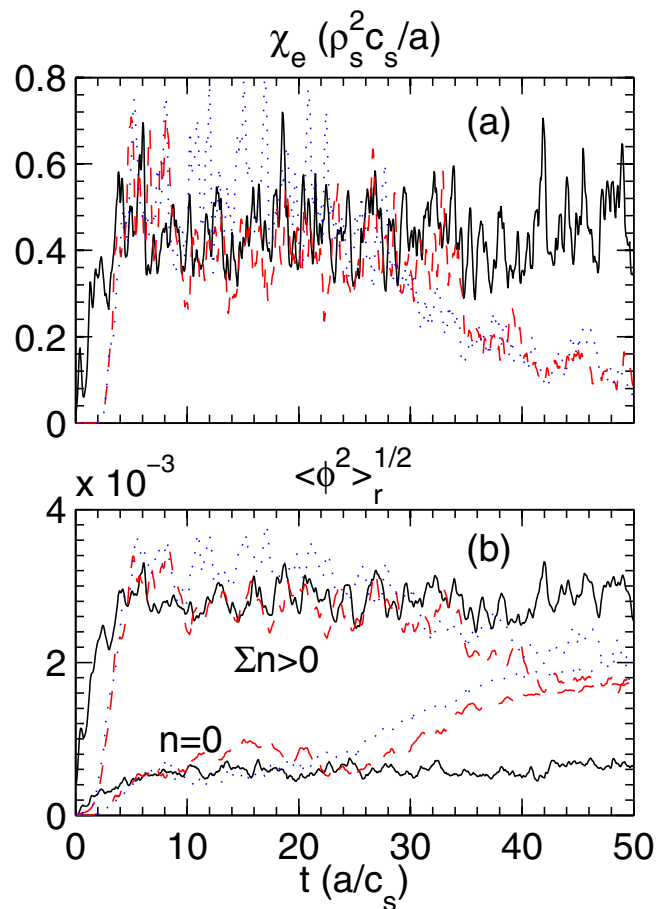


FIG. 6. (Color online) (a)  $\chi_e$  and (b) potential intensity for ETG-ki-exb (solid) and ETG-ai-exb (dashed) simulations. Increasing buffer damping strength to  $\nu^b=60c_s/a$  (dotted) does not eliminate the transport collapse.

$$\int d^3v \delta f_e = \delta n_e = \delta n_i = -n_0 \frac{e_i \delta \phi}{T_i}, \quad (3)$$

the interior zonal potential  $\delta \phi_{(n=0)}$  may be influenced by the damping of  $\delta f_{(n=0)}$  in the boundary regions. However, increasing the boundary damping dramatically from  $\nu^b=12c_s/a$  to  $60c_s/a$  ( $1.0v_{te}/a$ ) does not eliminate the corresponding collapse in transport, as shown in Fig. 6. We remark that the potential response in the ETG-ki-exb simulations always appears to reach temporal stationarity.

This failure of the ETG-ai-exb model to reproduce the ETG-ki-exb result is different to the lack of saturation observed in Ref. 18 for intermediate values of  $s$ , and we have observed this behavior in a number of ETG-ai-exb simulations using different combinations of box size, resolution, and buffer parameters. We note that the ETG-ai-exb simulations discussed in Ref. 14 never displayed a transition. In those simulations, the buffer regions were narrow but strongly damped ( $\Delta^b=16\rho_e$ ,  $\nu^b=60c_s/a$ ) and the full-radius adaptive source was enabled even though the simulations were local.

#### B. Reduced ion mass

Using smaller mass ratio reduces the number of modes required to span both ion and electron scales and can there-

fore reduce computational expense. But this reduction in separation between  $\rho_s$  and  $\rho_e$  scales can also lead to non-physical behavior. When varying  $\mu$  in multiscale simulations without  $E \times B$  shear<sup>16</sup> the total magnitude of  $\chi_e$  does not simply follow either ion gyroBohm ( $\chi_{GBs} = \rho_s^2 c_s / a$ ) or electron gyroBohm ( $\chi_{GBe} = \rho_e^2 v_{te} / a = \chi_{GBs} / \mu$ ) values. However, the transport spectra  $\chi_e / \chi_{GBe}$  does become invariant above  $k_\theta \rho_e > 0.1$ , although in this range its contribution can be relatively small (roughly 7%–15% of the total).

As strong  $E \times B$  shear suppresses ion-scale dynamics, it might be expected that  $\chi_e / \chi_{GBe}$  remains unchanged as ion mass is reduced. This expectation assumes that the electron dynamics are unaffected by the  $E \times B$  shear. However, it is important to consider that as  $\mu$  is varied, the  $E \times B$  shearing rate relative to the characteristic ion ( $c_s / a$ ) and electron ( $v_{te} / a$ ) rates will change. For instance, if  $\gamma_E(a / c_s)$  is held fixed,  $\gamma_E(a / v_{te}) = \gamma_E(a / c_s) / \mu$  will increase with reduced  $\mu$ . If  $\gamma_E$  is sufficiently small in electron units, this relative increase may have no effect on the resulting electron dynamics. Conversely, if  $\gamma_E(a / v_{te})$  is held fixed,  $\gamma_E(a / c_s) = \gamma_E(a / v_{te}) \mu$  will decrease, reducing the effectiveness of ion-scale suppression which could significantly alter the overall dynamics.

To clarify the effect of reduced ion mass, we perform simulations addressing the two scenarios above. The box sizes are fixed in ion units,  $(L_x, L_y) = (6, 2.2) \rho_i$ , while maintaining electron scale resolution with  $(k_\theta \rho_e)_{\max} = 1.5$  and  $(k_r \rho_e)_{\max} = 0.74$ . Note that when scaling  $\mu$ , the buffer widths are set to  $\Delta^b = 1.0 \rho_i$  with a damping rate of  $\nu^b = 6(c_s / a)$ . Unless otherwise noted, the perturbed gradient is less than 1% of the equilibrium. In the first scenario we maintain constant  $\gamma_E = 0.9(c_s / a)$ ,  $\gamma_p = (qR / r) \gamma_E = 4.0(c_s / a)$ , and  $\text{Ma} = 0.6$ . We find  $\chi_e / \chi_{GBi} = (0.448, 0.321, 0.214)$  for  $\mu = (60, 30, 20)$ . When measured in electron gyroBohm units, the reduction is even more dramatic:  $\chi_e / \chi_{GBe} = (26.9, 9.63, 4.28)$ . Perhaps unsurprisingly, the reduction in transport is consistent with a larger  $E \times B$  shear rate relative to the electron scale growth rates:  $\gamma_E(a / v_{te}) = \gamma_E(a / c_s) / \mu$ .

Figure 7 shows the fractional  $\chi_e$  spectra normalized in ion units [Fig. 7(a)] and electron units [Fig. 7(b)]. The location of transport peak does not remain centered at either a dominant ion or electron wavelength. This is in contrast to multiscale ITG-ETG simulations<sup>8</sup> where the ion scales are strongly driven in the absence of flow shear, and the transport spectra peak remains fixed around  $k_\theta \rho_s \approx 0.2$ – $0.25$  for  $\mu = 20, 30$ . The box size was doubled for both  $\mu = 20$  and 30 to verify convergence, with a small increase in transport of only 10% and 5%, respectively (thin lines in Fig. 7).

In this case the  $\mu$ -scan at fixed  $\gamma_E(a / c_s)$  is analogous to a scan in  $\gamma_E(a / v_{te})$  at constant  $\mu$ . This becomes apparent considering that the peak ETG growth rate is  $\gamma_{\text{lin}, \max} \approx 0.11 v_{te} / a$ , while  $\gamma_E = 0.9(v_{te} / a) / \mu$ , and therefore  $\gamma_E / \gamma_{\text{lin}, \max} \approx 0.14(60 / \mu)$ . As  $\mu$  is reduced from 60 to 20,  $\gamma_E / \gamma_{\text{lin}, \max}$  varies from roughly 0.14 to 0.42, and  $\chi_e / \chi_{GBe}$  from 27 to 4.3. This is similar to separate GS2 ETG-ai simulations (using different parameters) that demonstrated complete suppression of transport for  $\gamma_E / \gamma_{\text{lin}, \max}$  somewhere between 0.5 and 1.2.<sup>22</sup> These simulations illustrate

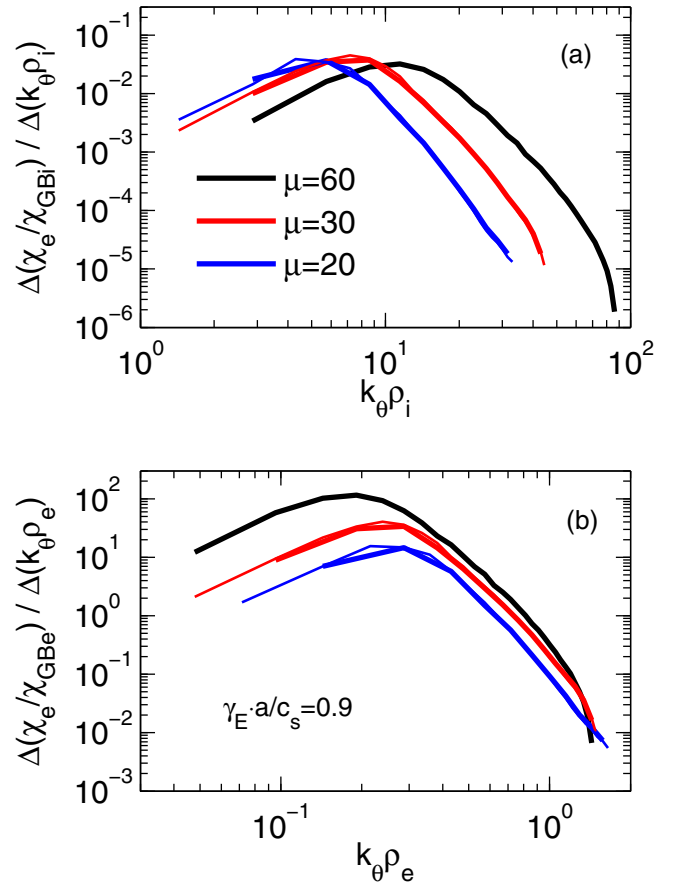


FIG. 7. (Color online) Fractional transport spectra normalized in (a) ion units and (b) electron units, from simulations with reduced mass ratio while fixing the  $E \times B$  shear rate in ion units ( $\gamma_E \cdot a / c_s = 0.9$ ).

that ETG transport is susceptible to suppression via  $E \times B$  shear, consistent with indications from recent turbulence measurements.<sup>12</sup>

To address the second scenario, an additional simulation was run for  $\mu = 30$  using  $\gamma_E(a / v_{te}) = 0.015$ , or equivalently,  $\gamma_E(a / c_s) = 0.45$ . The resulting  $\chi_e$  is  $0.934 \chi_{GBi}$ —about twice as large as the  $\mu = 60$  simulation but nearly identical in electron gyroBohm units:  $28 \chi_{GBe}$ . The fractional transport spectra (in electron units) in Fig. 8 shows that the  $\mu = 30$  simulation (two box sizes) reproduces the electron thermal transport. These simulations with strong  $E \times B$  shear relative to the ion dynamics demonstrate the same  $\mu$ -independent behavior for  $k_\theta \rho_s > 0.1$  as seen in the multiscale simulations with strongly driven ion-scale transport.

### C. Reduced $E \times B$ shear

The level of  $E \times B$  shear used in the above simulations was chosen to match the simulations in Ref. 8 where ETG-ai were converged with ETG-ki results for the Cyclone base case parameters. This value,  $\gamma_E = 0.45(c_s / a)$  at  $\mu = 30$ , is at the upper limit of experimental observations in MAST and NSTX. An additional simulation was carried out with  $\gamma_E = 0.3(c_s / a)$  at  $\mu = 30$ . The transport starts out larger than at  $\gamma_E = 0.45(c_s / a)$  [Fig. 9(a)], as would be expected, but drops to much smaller values at later times. This is correlated with

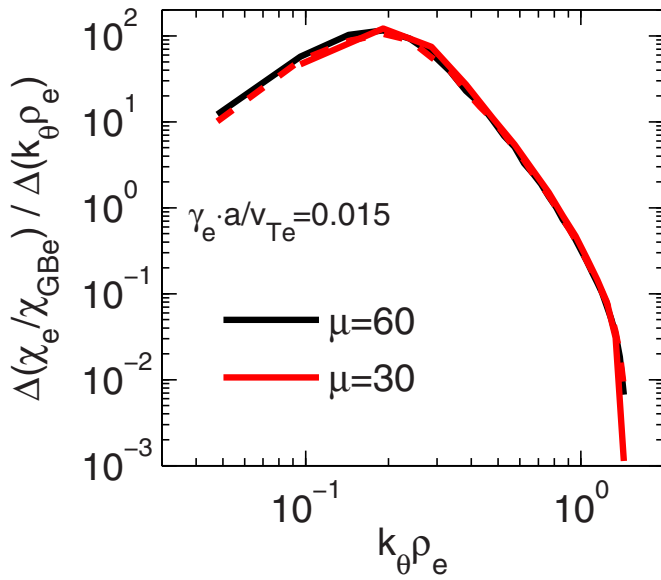


FIG. 8. (Color online) Fractional transport spectra in electron units for simulations using reduced mass ratio while keeping the  $E \times B$  shear rate fixed in electron units ( $\gamma_e(a/v_{te})=0.015$ ).

an increase in the zonal potential intensity, as shown in Fig. 9(b). An additional simulation at  $\gamma_E=0$  shows a transition that occurs much earlier on, and when using periodic BCs, actually takes the appearance of an initial transient of-

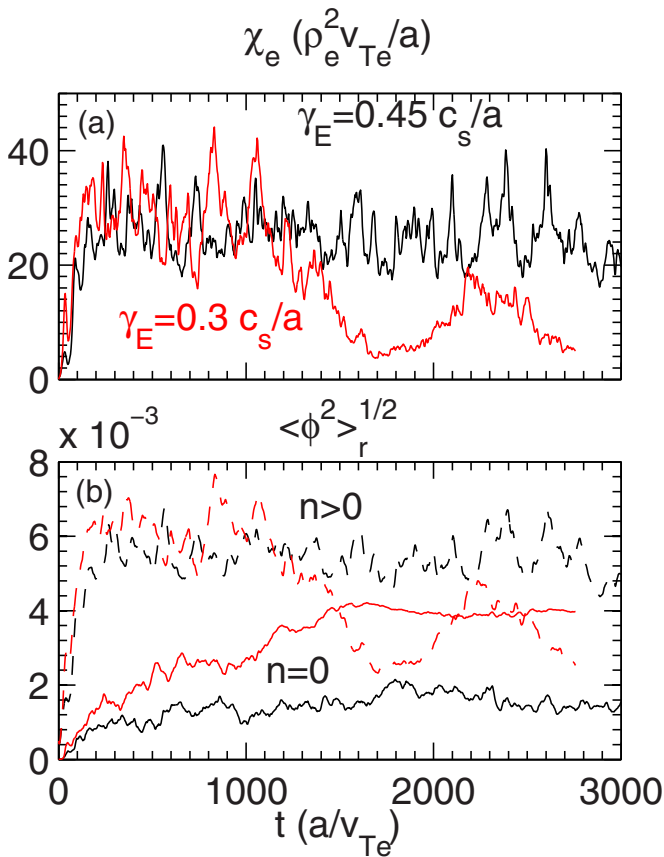


FIG. 9. (Color online) (a)  $\chi_e$  and (b) potential intensity vs time for simulations with reduced  $E \times B$  shear at mass ratio  $\mu=30$ .

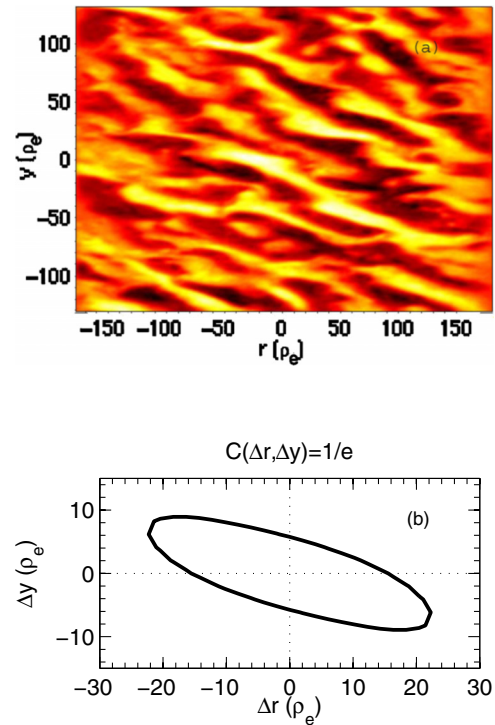


FIG. 10. (Color online) (a) Snapshot of density contours. (b)  $1/e$  contour of the 2D  $C(\Delta r, \Delta y)$  correlation function.

ten seen in simulations. For these reduced values of  $\gamma_E$  the box size is no longer large enough to capture physically relevant larger-scale ion dynamics.

#### IV. TURBULENCE CHARACTERISTICS

Lastly we discuss the corresponding turbulence characteristics of the ETG simulations relevant for STs. The fluctuation spectra are converged with respect to box size because of the large  $E \times B$  shear and should therefore be representative of physical spectra which can be used for comparison with diagnostic turbulence measurements.

Shown in Fig. 10(a) is a two-dimensional (2D) snapshot of the instantaneous density fluctuations from the simulation in Sec. II. The perturbations are tilted in the presence of the  $E \times B$  shear flow and appear to be extended in this tilted direction. This radially elongated structure, often referred to as a “streamer,”<sup>28</sup> is a remnant of the underlying linear instability that aligns itself so as to maximize transport. This elongated structure does not usually remain in analogous ITG nonlinear simulations because of the relatively stronger zonal flows that develop nonlinearly and isotropize the turbulence.<sup>29</sup>

The average eddy structure is evident in the perpendicular correlation function. Figure 10(b) shows the  $1/e$  contour of the 2D correlation function,  $C(\Delta x, \Delta y)=1/e$ , at the outboard midplane. The corresponding radial and binormal correlation lengths (at the  $1/e$  points) taken along the axes are  $L_x \approx 16\rho_e$  and  $L_y \approx 6\rho_e$ , and the correlation length along the tilted axis ( $\sim 20^\circ$ ) is  $L_\perp \approx 23\rho_e$ . These characteristic lengths are much smaller than the computational domain size,

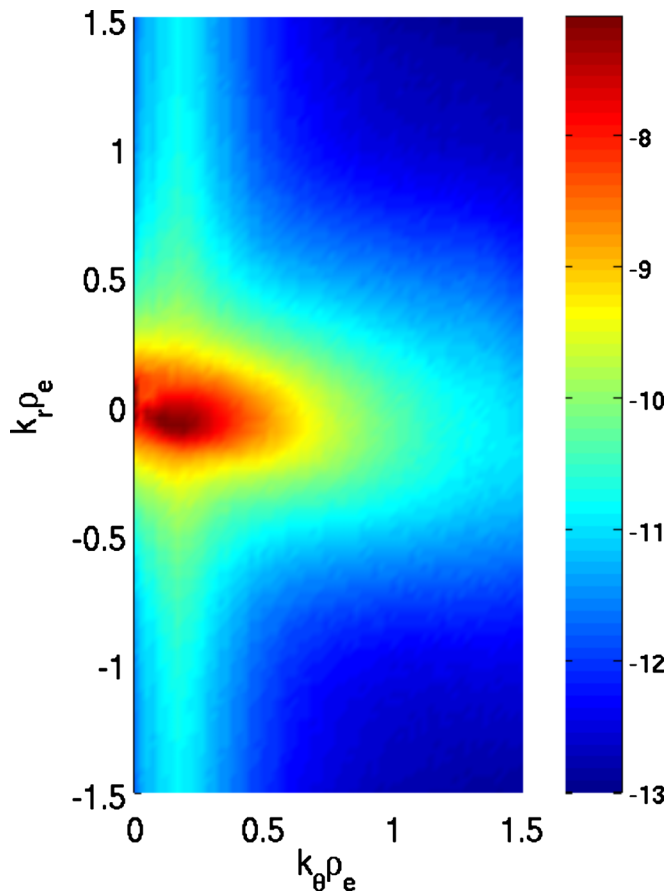


FIG. 11. (Color online) 2D wavenumber spectra corresponding to Fig. 10.

$L_x \times L_y = 360 \times 260 \rho_e$ , consistent with convergence in box size, and are also shorter than the appearance of the instantaneous eddy structures in Fig. 10(a).

While not unique from the correlation function, it is useful to inspect the 2D power spectra as turbulence diagnostics often measure quantities most directly related to this. Figure 11 shows the electron density power spectra (at the outboard midplane) corresponding to the correlation function in Fig. 10. When  $k_{\perp} \rho_e < 0.2$ , the anisotropy characteristic of the radially elongated eddies in the ETG turbulence is apparent. Specifically, the strongest fluctuations occur for  $k_{\theta} \rho_e \approx 0.15$  and  $k_r \rho_e \approx 0.05$ . Surprisingly at higher wavenumbers,  $k_{\perp} \rho_e > 0.2$ , the spectrum remains anisotropic, in contrast to the spectra reported in previous ETG simulations without  $E \times B$  shear.<sup>16,18</sup>

The influence of the  $E \times B$  shear is evident as the spectrum peak shifts to finite  $k_r$  at increasing  $k_{\theta}$ , roughly analogous to the tilted correlation function. This is illustrated by the mean value of  $\langle k_r \rangle$  calculated using the simulated power spectra at each  $k_{\theta}$ . This shift in  $\langle k_r \rangle$  roughly follows  $k_{\theta} \gamma_E / \Delta \omega_T$ , where  $\Delta \omega_T$  is the inverse correlation time of a given  $k_{\theta}$  mode determined from the spectral width of the  $k_{\theta} \omega$  spectra at each  $k_{\theta}$ .

The anisotropy exhibited across all scales in the simulated 2D ETG spectra has implications for the interpretation of turbulence diagnostics. For instance, the recently reported high- $k$  scattering measurements on NSTX observe perpen-

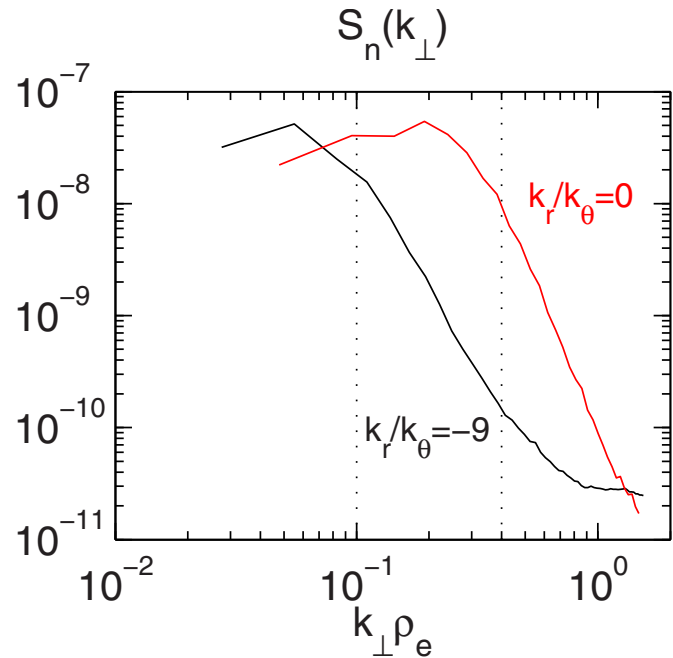


FIG. 12. (Color online) Density spectra vs  $k_{\perp}$  for different ratios of  $(k_r/k_{\theta})$ .

dicular wavenumbers  $k_r/k_{\theta}$  in the range of 9 to 10.<sup>11</sup> Figure 12 shows one-dimensional (1D)  $k_{\perp}$  spectra determined by interpolating from the 2D spectra in Fig. 11 at fixed ratios of  $k_r/k_{\theta} = -9$  and 0. In the range of measurable wavenumbers (0.1–0.4)<sup>11</sup> the 1D spectra exhibit different relative shapes with a strong spectral decay ( $k_{\perp}^{-\alpha}$  with  $\alpha \approx 3.5$ ) apparent in the case of  $k_r/k_{\theta} = -9$ . In contrast to this, a local peak at  $k_{\perp} \rho_e = 0.2$  is observed for  $k_r/k_{\theta} = 0$  which corresponds to the region in  $k_{\theta} \rho_e$  where transport dominates (see Fig. 3). In addition, the spectral intensity is up to two orders of magnitude larger for the case of  $k_r/k_{\theta} = 0$ .

The level of anisotropy and the location of the spectrum peak  $(k_r, k_{\theta})_{\text{peak}}$  may change depending on the strength of  $E \times B$  shear, which could be altered by varying the toroidal momentum injection (using different combinations of heating sources) or braking the plasma with applied magnetic field perturbations.<sup>30</sup> Ultimately, synthetic diagnostics<sup>31</sup> must be applied to these simulations to make a direct comparison with measurements and to determine whether the above anisotropy is smoothed out by the instrument function of a particular diagnostic.

## V. SUMMARY

ETG turbulence remains a plausible explanation for anomalous electron thermal transport in at least some spherical tokamak experiments. As such, nonlinear ETG simulations specifically relevant to STs are required for validation with experimental transport analysis, turbulence measurements, and reduced transport models. For neutral-beam-heated plasmas with large toroidal flow, these simulations must include the strong  $E \times B$  shear to provide a physical long-wavelength cutoff that exists experimentally. In the absence of such a cutoff, multiscale simulations are required to obtain convergence with computational domain size.

In this paper we have presented a number of nonlinear ETG simulations using reference ST parameters that include  $E \times B$  shear and kinetic ions to obtain well-behaved saturated results. Convergence with respect to BCs, numerical resolution and physical domain size was demonstrated. The resulting predicted transport is significant (roughly  $0.4\rho_s^2 c_s/a$ ) and well within the range of experimental observations in both MAST and NSTX.

In the presence of strong  $E \times B$  shear the computationally cheaper adiabatic ion model was found to be unreliable, although its mode of failure differs from that observed in ETG-ai simulations in the absence of  $E \times B$  shear. When using reduced mass ratio, the influence of  $E \times B$  shear depends on whether it is held constant with respect to ion or electron time scales. In the reference case at large  $\gamma_E$ , the resulting transport in electron units ( $\chi_e/\chi_{GBe}$ ) is unchanged if  $\gamma_E(a/v_{te}) = \gamma_E(a/c_s)\mu$  (or equivalently,  $\gamma_E/\gamma_{lin}$ ) is held fixed. On the other hand, if  $\gamma_E(a/c_s)$  is held fixed,  $\gamma_E/\gamma_{lin}$  increases and the resulting transport is reduced, demonstrating that ETG turbulence is indeed susceptible to suppression via sheared  $E \times B$  flows.

Finally, electron scale turbulence characteristics were presented for the converged simulations. Elongated eddy structures are observed but are tilted in the sheared flow field. The corresponding intensity spectra is anisotropic across all simulated length scales ( $k_r, k_\theta$ ) which must be accounted for when interpreting turbulence measurements in this wavenumber range.

## ACKNOWLEDGMENTS

We gratefully acknowledge helpful discussions with C. S. Brady, R. O. Dendy, A. R. Field, D. R. Mikkelsen A. G. Peeters, F. M. Poli, C. M. Roach, and M. Valovič. Calculations were performed at the University of Warwick Centre for Scientific Computing, HECToR (EPSRC Grant EP/H002081/1), and NERSC.

- <sup>1</sup>R. J. Akers, J. W. Ahn, G. Y. Antar, L. C. Appel, D. Applegate, C. Brickley, C. Bunting, P. G. Carolan, C. D. Challis, N. J. Conway, G. F. Counsell, R. O. Dendy, B. Dudson, A. R. Field, A. Kirk, B. Lloyd, H. F. Meyer, A. W. Morris, A. Patel, C. M. Roach, V. Rohzansky, A. Sykes, D. Taylor, M. R. Tourmianski, M. Valovic, H. R. Wilson, K. B. Axon, R. J. Buttery, D. Ciric, G. Cunningham, J. Dowling, M. R. Dunstan, S. J. Gee, M. P. Gryaznevich, P. Helander, D. L. Keeling, P. J. Knight, F. Lott, M. J. Loughlin, S. J. Manhood, R. Martin, G. J. McArdle, M. N. Price, K. Stammers, J. Storrs, M. J. Walsh, and MAST and NBI Team, *Plasma Phys. Controlled Fusion* **45**, A175 (2003).
- <sup>2</sup>A. R. Field, R. J. Akers, D. J. Applegate, C. Brickley, P. G. Carolan, C. Challis, N. J. Conway, S. C. Cowley, G. Cunningham, N. Joiner, H. Meyer, A. Patel, C. Roach, M. Valovič, M. J. Walsh, and the MAST team, Proceedings of the 20th IAEA Fusion Energy Conference, Vilamoura, Portugal, 2004, pp. EX/P2-11 (2004).
- <sup>3</sup>S. M. Kaye, F. M. Levinton, D. Stutman, K. Tritz, H. Yuh, M. G. Bell, R. E. Bell, C. W. Domier, D. Gates, W. Horton, J. Kim, B. P. LeBlanc, N. C.

- Luhmann Jr., R. Maingi, E. Mazzucato, J. E. Menard, D. Mikkelsen, D. Mueller, H. Park, G. Rewoldt, S.A. Sabbagh, D. R. Smith, and W. Wang, *Nucl. Fusion* **47**, 499 (2007).
- <sup>4</sup>J. Kinsey, R. Waltz, and J. Candy, *Phys. Plasmas* **12**, 062302 (2005).
- <sup>5</sup>J. Kinsey, R. Waltz, and J. Candy, *Phys. Plasmas* **14**, 102306 (2007).
- <sup>6</sup>D. Stutman, L. Delgado-Aparicio, N. Gorelenkov, M. Finkenthal, E. Fredrickson, S. Kaye, E. Mazzucato, and K. Tritz, *Phys. Rev. Lett.* **102**, 115002 (2009).
- <sup>7</sup>F. Jenko, *J. Plasma Fusion Res, SERIES* **6**, 11 (2004).
- <sup>8</sup>J. Candy, R. Waltz, M. Fahey, and C. Holland, *Plasma Phys. Controlled Fusion* **49**, 1209 (2007).
- <sup>9</sup>J. Candy, *Plasma Phys. Controlled Fusion* **51**, 105009 (2009).
- <sup>10</sup>E. Mazzucato, D. R. Smith, R. E. Bell, S. M. Kaye, J. C. Hosea, B. P. LeBlanc, J. R. Wilson, P. M. Ryan, C. W. Domier, N. C. Luhmann Jr., H. Yuh, W. Lee, and H. Park, *Phys. Rev. Lett.* **101**, 075001 (2008).
- <sup>11</sup>E. Mazzucato, R. E. Bell, S. Ethier, J. C. Hosea, S. M. Kaye, B. P. LeBlanc, W. W. Lee, P. M. Ryan, D. R. Smith, W. X. Wang, J. R. Wilson, and H. Yuh, *Nucl. Fusion* **49**, 055001 (2009).
- <sup>12</sup>D. R. Smith, S. M. Kaye, W. Lee, E. Mazzucato, H. K. Park, R. E. Bell, C. W. Domier, B. P. LeBlanc, F. M. Levinton, N. C. Luhmann Jr., J. E. Menard, and H. Yuh, *Phys. Rev. Lett.* **102**, 225005 (2009).
- <sup>13</sup>W. Horton, H. Wong, P. Morrison, A. Wurm, J. Kim, J. Perez, J. Prat, G. Hoang, B. LeBlanc, and R. Bell, *Nucl. Fusion* **45**, 976 (2005).
- <sup>14</sup>R. J. Akers, D. J. Applegate, J. Candy, G. Colyer, D. Dunai, A. R. Field, W. Guttenfelder, J. E. Kinsey, M. Reshko, C. M. Roach, S. Saarelma, G. E. Staebler, A. Thyagaraja, M. Valovič, R. E. Waltz, S. Zoletnik, O. Zolotukhin, and the MAST team, Proceedings of the 22nd IAEA Fusion Energy Conference, Geneva, Switzerland, 2008, pp. EX/2-2.
- <sup>15</sup>G. Staebler, G. Colyer, S. Kaye, J. Kinsey, and R. Waltz, Proceedings of the 22nd IAEA Fusion Energy Conference, Geneva, Switzerland, 2008, pp. TH/P8-42.
- <sup>16</sup>R. Waltz, J. Candy, and M. Fahey, *Phys. Plasmas* **14**, 056116 (2007).
- <sup>17</sup>T. Görler and F. Jenko, *Phys. Rev. Lett.* **100**, 185002 (2008).
- <sup>18</sup>W. M. Nevins, J. Candy, S. Cowley, T. Dannert, A. Dimits, W. Dorland, C. Estrada-Mila, G. W. Hammett, F. Jenko, M. J. Pueschel, and D. E. Shumaker, *Phys. Plasmas* **13**, 122306 (2006).
- <sup>19</sup>W. Nevins, S. Parker, Y. Chen, J. Candy, A. Dimits, W. Dorland, G. Hammett, and F. Jenko, *Phys. Plasmas* **14**, 084501 (2007).
- <sup>20</sup>A. Peeters, Y. Camenen, F. Casson, W. Hornsby, A. Snodin, D. Strintzi, and G. Szepesi, *Comput. Phys. Commun.* **180**, 2650 (2009).
- <sup>21</sup>N. Joiner, D. Applegate, S. Cowley, W. Dorland, and C. Roach, *Plasma Phys. Controlled Fusion* **48**, 685 (2006).
- <sup>22</sup>C. M. Roach, I. G. Abel, R. J. Akers, W. Arter, M. Barnes, Y. Camenen, F. J. Casson, G. Colyer, J. W. Connor, S. C. Cowley, D. Dickinson, W. Dorland, A. R. Field, W. Guttenfelder, G. W. Hammett, R. J. Hastie, E. Highcock, N. F. Loureiro, A. G. Peeters, M. Reshko, S. Saarelma, A. A. Schekochihin, M. Valovic, and H. R. Wilson, *Plasma Phys. Controlled Fusion* **51**, 124020 (2009).
- <sup>23</sup>J. Candy and R. Waltz, *J. Comput. Phys.* **186**, 545 (2003).
- <sup>24</sup>J. Candy and E. Belli, General Atomics Technical Report No. GA-A26818 (2010).
- <sup>25</sup>R. Miller, M. Chu, J. Greene, Y. Lin-liu, and R. Waltz, *Phys. Plasmas* **5**, 973 (1998).
- <sup>26</sup>J. Candy and R. Waltz, *Phys. Plasmas* **13**, 032310 (2006).
- <sup>27</sup>R. Waltz, J. Candy, and M. Rosenbluth, *Phys. Plasmas* **9**, 1938 (2002).
- <sup>28</sup>F. Jenko, W. Dorland, M. Kotschenreuther, and B. Rogers, *Phys. Plasmas* **7**, 1904 (2000).
- <sup>29</sup>F. Jenko and W. Dorland, *Phys. Rev. Lett.* **89**, 225001 (2002).
- <sup>30</sup>S. Kaye, W. Solomon, R. Bell, B. LeBlanc, F. Levinton, J. Menard, G. Rewoldt, S. Sabbagh, W. Wang, and H. Yuh, *Nucl. Fusion* **49**, 045010 (2009).
- <sup>31</sup>F. Poli, S. Ethier, W. Wang, T. Hahm, E. Mazzucato, and D. Smith, *Phys. Plasmas* **17**, 112514 (2010).